CrossMark

Novel highly ordered core–shell nanoparticles

Sonal Dey[1,4,*] ⓘ, Mohammad D. Hossain[1], Robert A. Mayanovic[1], Richard Wirth[2], and Robert A. Gordon[3,5]

[1] *Department of Physics, Astronomy & Materials Science, Missouri State University, Springfield, MO 65897, USA*

[2] *GeoForschungsZentrum Potsdam, Department 3.3, Telegrafenberg, 14473 Potsdam, Germany*

[3] *PNCSRF, APS Sector 20, Argonne, IL, USA*

[4] *Present address: Colleges of Nanoscale Science and Engineering, State University of New York Polytechnic Institute, Albany, NY 12203, USA*

[5] *Present address: Moyie Institute, Coquitlam, BC, Canada*

ABSTRACT

Core–shell nanoparticles have potential for a wide range of applications due to the tunability of their magnetic, catalytic, electronic, optical, and other physicochemical properties. A frequent drawback in the design of core–shell nanoparticles and nanocrystals is the lack of control over an extensive, disordered, and compositionally distinct interface that occurs due to the dissimilarity of structural and compositional phases of the core and shell. In this work, we demonstrate a new hydrothermal nanophase epitaxy (HNE) technique to synthesize highly structurally ordered $\alpha\text{-}Cr_2O_3@\alpha\text{-}Co_{0.38}Cr_{1.62}O_{2.92}$ inverted core–shell nanoparticles (CSNs) with evidence for the nanoscale growth of corundum structure beginning from the core and extending completely into the shell of the CSNs with minimal defects at the interface. The high-resolution TEM results show a sharp interface exhibiting epitaxial atomic registry of shell atoms over highly ordered core atoms. The XPS and Co K-edge XANES analyses indicate the +2 oxidation state of cobalt is incorporated in the shell of the CSNs. Our XPS and EXAFS results are consistent with oxygen vacancy formation in order to maintain charge neutrality upon substitution of the Co^{2+} ion for the Cr^{3+} ion in the $\alpha\text{-}Co_{0.38}Cr_{1.62}O_{2.92}$ shell. Furthermore, the CSNs exhibit the magnetic exchange bias effect, which is attributed to the exchange anisotropy at the interface made possible by the nanophase epitaxial growth of the $\alpha\text{-}Co_{0.38}Cr_{1.62}O_{2.92}$ shell on the $\alpha\text{-}Cr_2O_3$ core of the nanoparticles. The combination of a well-structured, sharp interface and novel nanophase characteristics is highly desirable for nanostructures having enhanced magnetic properties.

Address correspondence to E-mail: deysonal2012@gmail.com

Introduction

Core–shell nanoparticles are currently of considerable interest because their physicochemical properties are tunable by varying the core vs shell size, chemical composition, interface characteristics, and atomic-scale structure. This tunability has resulted in the ability to target a wide range of applications of core–shell nanostructures, including those in optics, catalysis, medicine, and energy storage [1–6]. Magnetic core–shell nanoparticles are of particular interest because of their potential applications in magnetic random-access memory, spintronic devices, cell separation, tissue engineering, drug delivery, MRI-targeted cell imaging, and hyperthermia [7–10]. The increasing complexity of core–shell nanoparticles/nanocrystals (e.g., shape, type, and arrangement), which is owed to the tremendous advances in chemical synthesis methodologies, has led not only to a high degree of control in the nature of targeted properties but also in the potential to tailor multi-functionality, such as having a combination of magnetic and catalytic properties.

Core–shell nanoparticles (CSNs) having distinct magnetic phases (in the core vs the shell) that interact via the exchange bias effect (possibly due to exchange anisotropy at the interface) are presently extensively studied due to their potential industrial and medical applications [7–10]. An important structural aspect of CSNs is that the structure of the core and shell are typically dissimilar. This structural incompatibility typically results in considerable structural disorder, lattice defect formation, amorphization, and roughness at the interface between the core and shell. The disorder, defects, roughness, and extent of the interface relative to the sizes of the core and shell can have a strong but as yet not fully understood effect on the nature and extent of the exchange bias effect in CSNs. Experimental studies have shown that substantial structural disorder at the interface leads to a reduction in the exchange bias in $Fe_2O_3@Mn_3O_4$ [10] and of Co@CoO CSNs [11]; experimental results have also shown that interface roughness reduces exchange bias in $CoO@Fe_3O_4$ core–shell nanocrystallites [12]. Similarly, Monte Carlo simulations show that the presence of structural disorder [13], vacancies [14], and roughness [15] at the interface degrades the exchange bias. However, other calculations show that the magnitude of the exchange bias field is strongly coupled to the degree of interface roughness in FM@AFM CSNs [16]. Furthermore, complications can arise in experimentally resolving the effects due to dipolar inter-particle interactions, shape of nanoparticles, nanocrystalline faceting, nanoparticle size, and extent of core vs shell from those stemming from structural disorder, defects, and roughness at the core–shell interface. Progress in this area of nanoscience is complicated by the lack of atomic-scale control on the level of defects, roughness, and structural disorder at the interface of two-phase core–shell nanoparticles (NPs) and nanocrystals.

Our group has devised a novel hydrothermal nanophase epitaxy (HNE) technique for synthesis of crystalline CSNs having well-ordered interfaces. By mimicking natural processes of mineral zoning formation under hydrothermal conditions [17, 18], we are able to incorporate transition elements (M) into a highly structurally ordered Cr_2O_3-based shell, to form α-$Cr_2O_3@\alpha$-$M_xCr_{2-x}O_y$ inverted CSNs. The inverted CSNs, having an AFM core and a FM or ferrimagnetic (FiM) shell, are of interest because of their easier tunability resulting in enhanced magnetic properties [19, 20]. The advantages offered by our HNE method are the production of highly structured, epitaxial CSNs with minimal core-to-shell interface strain and roughness effects and purposeful introduction of oxygen vacancies on and near the surface of the NPs. Our synthesis offers a benign chemical route for the production of novel oxide CSNs having substantially enhanced physical (e.g., magnetic and optical) and chemical properties. Such nanomaterials may be optimally suited for tailored, multifunctional applications (e.g., magnetic and photocatalytic). In this work, we report the first synthesis and characterization of a novel epitaxial α-$Co_{0.38}Cr_{1.62}O_{2.92}$ nanophase shell overgrown on the α-Cr_2O_3 core of the CSNs, using our HNE technique.

Experimental

Preparation of the CSNs

The Cr_2O_3 NPs used in this study were synthesized following the procedures outlined elsewhere [21]. A 0.2 m solution of commercially available $Cr(NO_3)_3 \cdot 9H_2O$ (Sigma-Aldrich) was prepared and then mixed with an organic surfactant Triethanolamine (TEOA) in 1:2 molar ratio. The solution

was magnetically stirred for approximately 1 h and then placed under microwave irradiation for 5 min. Then, the solution was placed on top of a bar magnet and a dark-green colored precipitate collected at the bottom after approximately 6 h. The precipitate was separated from the solution and then dried in air. Next, the precipitate was calcined in air at 575 °C for 2 h. The sample turned into a green-colored fine powder at the conclusion of the calcination process. The Cr_2O_3 NPs were characterized using X-ray diffraction (XRD) and transmission electron microscopy (TEM) techniques.

Commercially available $CoCl_2$ (Online Science Mall) was dissolved in deionized water (deoxygenated by passing N_2 gas for 15 min) to prepare a 0.05 m aqueous solution (pH = 6.1) of $CoCl_2$. Cr_2O_3 NPs were added at a quantity of 0.09 g to 10 ml of the $CoCl_2$ solution. The solution was sonicated for ~15 min immediately after preparation and also before loading into our high-temperature Hastelloy C-276 hydrothermal reactor [22], in order to perform the hydrothermal nanophase epitaxy. The NPs and aqueous solution mixture was heated to ~205 °C and held at that temperature for ~17 h before cooling to room temperature, in order to grow the CSNs. After the HNE, the CSNs were rinsed using DI water and a centrifuge and dried on a glass plate in air at 25 °C. Figure S1 in the Electronic Supplementary Materials (ESM) shows a schematic model of the CSNs.

Scanning electron microscopy (SEM)

The scanning electron microscopy (SEM) imaging and SEM energy-dispersive X-ray spectroscopy (EDX) measurements were made on the α-Cr_2O_3@α-$Co_xCr_{2-x}O_y$ CSNs using an FEI Quanta 200, operating at 20 kV. The powder Cr_2O_3 NPs were spread on a conducting carbon tape under the SEM. Figure 1a and b show the SEM and SEM-EDX results for the CSNs, respectively.

Transmission electron microscopy (TEM)

TEM images of the α-Cr_2O_3 and α-Cr_2O_3@α-$Co_{0.38}$ $Cr_{1.62}O_{2.92}$ inverted core–shell NPs were collected at the GeoForschungZentrum using a TECNAI G2 F20 X-Twin microscope. The field emission gun of the TEM was operated at 200 keV. High-resolution lattice fringe images were acquired with a Gatan imaging
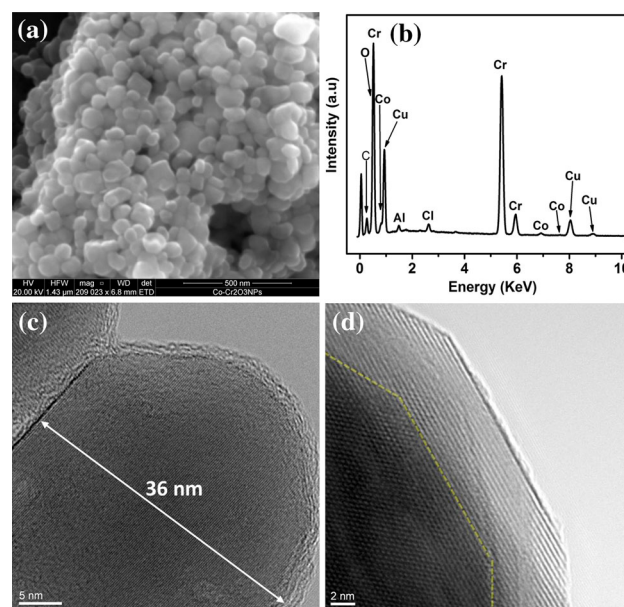

Figure 1 **a** An SEM image of the core–shell nanoparticles (CSNs); **b** SEM-EDX data collected from a single CSN; **c** a HR-TEM image of α-Cr_2O_3 NPs (core) with the approximate diameter of the core (~36 nm) indicated in the image; **d** a HR-TEM image of an individual CSN. The *yellow dashed line* in (**d**) indicates the location of the interface between the core (*darker region*) and shell (*lighter*, peripheral) region of the CSN.

filter (GIF Tridiem) as energy filtered images applying a 20 eV window to the zero-loss peak. Diffraction patterns were calculated from the high-resolution lattice fringe images using fast Fourier transform (FFT) from the digital micrograph inside the ImageJ software package. Figure 1c and d show the HR-TEM images of the core and the CSN, respectively. Figure 2 shows the TEM and TEM-EDX results. Additional TEM images are shown in Fig. S2 in the ESM. A more detailed analysis of the HR-TEM image of Fig. 2 is presented in Fig. S3 in the ESM.

X-ray diffraction (XRD)

Room temperature X-ray diffraction (XRD) measurements ($\theta - 2\theta$ scan) were made on the as-prepared α-Cr_2O_3 NPs and the α-Cr_2O_3@α-$Co_xCr_{2-x}O_y$ CSNs with a powder diffractometer (Bruker D8 Discover) using Cu Kα radiation from a sealed tube operating at 40 kV and 30 mA. A Göbel mirror and a 0.6 mm slit were used in the incident side of the X-ray beam followed by a 0.6 mm slit on the side of the diffracted beam. Structural parameters were extracted from the XRD patterns using the Bruker
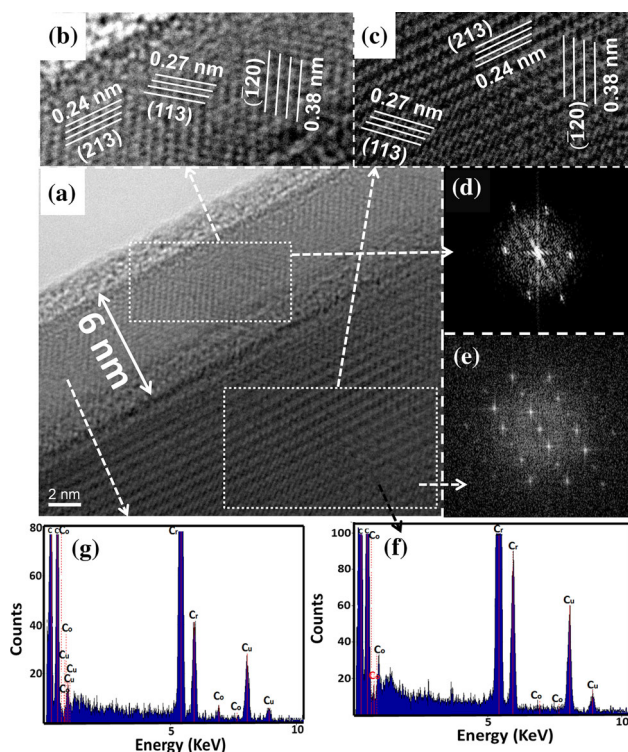
Figure 2 a An HR-TEM image of a single CSN showing the core (*lower*) and shell (*upper*; ∼6 nm wide); Select lattice planes (labeled) of the **b** shell and **c** core regions shown; **d**, **e** the FFTs of the regions of the shell and core as shown in (**b**, **c**) respectively; the TEM-EDX of the (**f**) core and (**g**) shell regions.
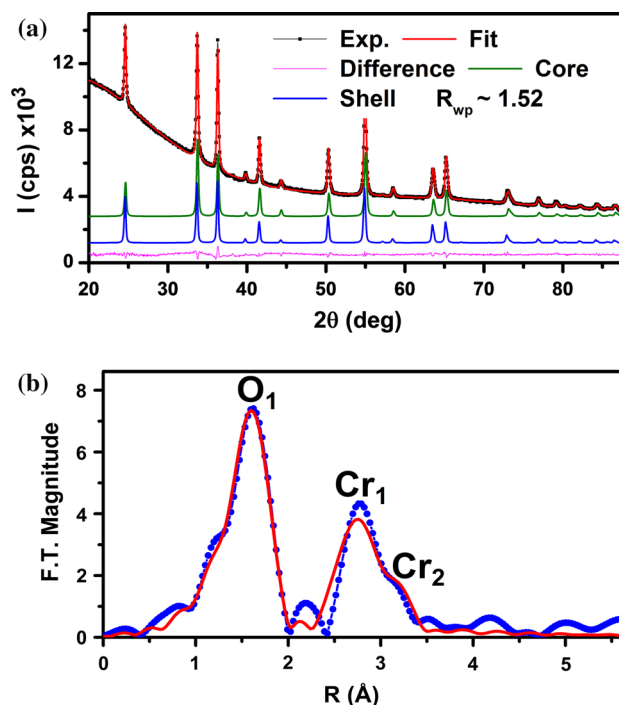

Figure 3 **a** The Rietveld refinement of the XRD data measured from the CSNs. Both the core and shell have a corundum structure (space group #167:R$\bar{3}$c). The *asterisk* indicates an impurity peak. **b** The Fourier transform (FT) of the isolated oscillations of the EXAFS data (*blue line + solid circles*) and the fit (*red line*) to the data.

TOPAS full-pattern refinement program [23–25]. The zero error and incident beam profile of the instrument were determined using a modified Thompson-Cox-Hastings pseudo-Voigt peak function (TCHZ) [26] from a NIST 674b standard reference material (CeO$_2$). The peak asymmetry due to axial divergence of the beam was modeled using the NIST 674b CeO$_2$ standard based on work by Finger et al. [27] The zero error of the instrument, parameters of the TCHZ peak function describing the incident beam profile, and axial divergence of the beam were fixed during the subsequent structural refinement of the samples. The background function for the XRD pattern was modeled using a Chebyshev Polynomial of 5-th order [23]. The amorphous-like background of the XRD data from α-Cr$_2$O$_3$@α-Co$_x$Cr$_{2−x}$O$_y$ NPs (Fig. 3) came from the glass substrate used to hold the particles and was modeled using a broad Voigt function. A non-linear least square fitting method was performed to minimize the value of "R-weighted pattern" (R_{wp}) during Rietveld refinement.

Symmetry-mode Rietveld refinement [28–30] was made on both the as-prepared α-Cr$_2$O$_3$ NPs and the α-Cr$_2$O$_3$@α-Co$_x$Cr$_{2−x}$O$_y$ CSNs with a corundum structure (space group #167) based on ICSD #261801 as the starting structure. Figures 3 and S4 show the Rietveld refinement results for the α-Cr$_2$O$_3$@α-Co$_x$Cr$_{2−x}$O$_y$ CSNs and the α-Cr$_2$O$_3$ core NPs, respectively. Table S1 summarizes the results of the Rietveld refinement.

XAS measurements

Co *K*-edge XAS measurements were performed on the α-Cr$_2$O$_3$@α-Co$_{0.38}$Cr$_{1.62}$O$_{2.92}$ inverted core–shell NPs at the PNC/XSD beam line 20-BM-B at the Advanced Photon Source (APS). The XAS spectra were measured in fluorescence mode using a 13-element Ge solid-state detector. The APS synchrotron was operated at an energy of 7.0 GeV with a maximum fill current of 100 mA (in 324 bunches). The incident X-ray beam flux at the 20-BM-B beam line was ∼2 × 10^9 photons/second measured using an

N_2-filled transmission chamber kept before the sample. The Si(111) double-crystal monochromator was detuned by 20 % 300 eV above the Co edge and a Rh-coated harmonic rejection mirror was also used. Cobalt K-edge calibration was accomplished using cobalt metal foil. The overall spectrum used during the data analyses was averaged from 60 individual scans.

EXAFS data analysis

Reduction of the XAS spectrum was carried out using ATHENA1.2 software [31]. The nonlinear least squares fitting of the χ data, which are the isolated extended X-ray absorption fine structure (EXAFS) oscillations, was made using IFEFFIT0.9 [32]. The k^3-weighted χ data were Fourier transformed in the 3.0–13.0 Å^{-1} k-space range. The Fourier-transformed (FT) χ data were fit in R-space, in the 1.3–3.5 Å range using theoretical XAS curves generated with FEFF9 [33]. An orthorhombic corundum-type structure (space group #167) model consisting of 58 atoms was used in the theoretical XAS calculation. The structure model consists of the Co atom at the center with Cr and O atoms occupying the remaining sites. In reality, there are additional Co in the outer shells surrounding the central Co atom in the α-Cr_2O_3@α-$Co_{0.38}Cr_{1.62}O_{2.92}$ CSNs. However, Co–Co scattering was not explicitly taken into account, by use of a separate scattering path, in order to simplify the analysis. Three single scattering Co-A (A = O, Cr) paths, generated using FEFF9, were used to fit the Co K-edge χ data. The fitting parameters include the coordination number (N), the radial distance (R), the mean-square relative displacement (MSRD: σ^2) of the XAS Debye–Waller factor, and ΔE_0, for each path. ΔE_0 is defined as the difference between the calculated Fermi level and the absorption edge position as determined by the main peak in the first derivative of the absorption. An amplitude normalization factor $S_0^2 = 0.7$ was used in the calculation of the coordination number N of each path. The goodness of fit parameter (R_{fit}) as implemented in IFFEFIT was 0.034.

XANES data analysis

After processing, the XANES were isolated from the XAS spectra and normalized with respect to the individual step height values. The ab initio XANES

calculations were made using FEFF9.[24] The atomic cluster model utilized in the calculations consists of a central Co atom surrounded by Cr, Co, and O atoms simulating an α-$Co_{0.5}Cr_{1.5}O_3$ corundum structure of 58 atoms. The Co K-edge XANES and the associated angular momentum projected density of states (l-DOS) calculations were made simultaneously. The self-consistent field (SCF) potential calculations utilized Hedin–Lundqvist [34] potentials and were made in full multiple scattering mode. A dispersion value of 0.2 eV was used in the calculations to simulate the effects of instrument and core–hole lifetime broadening. The discontinuities between adjacent regions of the muffin-tin potentials were reduced by a slight overlap via an AFOLP value of 1.09. A mean-square relative disorder parameter of the Debye–Waller factor of 0.016 Å^{-1} was used in the calculations.

X-ray photoelectron spectroscopy (XPS)

Compositional analysis of the sample was made using X-ray photoelectron spectroscopy (XPS). Twin crystal monochromatic Al K-alpha with a characteristic energy of 1486.6 eV was used as a source of X-rays. The Ag $3d_{5/2}$ (FWHM = 0.36 eV) peak with a characteristic energy of 368.26 eV was used for calibration of the source and analyzer. The XPS data were collected using a Thermo Scientific Alpha 110 hemispherical analyzer with pass energy of 25 eV. The CasaXPS 2.3.16 software was used for analysis and peak fitting of the XPS spectra. The high-resolution scans, including the survey scan, were calibrated with respect to the C 1s peak (284.8 eV). A Shirley background within the CasaXPS software was used in the fitting of the XPS peaks in the survey scan in the high-resolution spectra. A Gaussian–Lorentzian product GL(30) function was used for relatively symmetric line shapes, whereas a Lorentzian functional form convoluted with a Gaussian LA(a,b,n) function was used in the fitting of asymmetric line shapes of the high-resolution peaks. The XPS results are summarized in section S4 of the ESM.

Magnetic measurements

The magnetic hysteresis measurements, both in zero field cooled (ZFC) and field cooled (FC) mode, were made using a Quantum Design SQUID MPMS/XL magnetometer in a magnetic field in the ±50 kOe

Table 1 Summary of structural results obtained from fitting of the Co K-edge EXAFS measured from the α-Cr_2O_3@α-$Co_xCr_{2-x}O_y$ core–shell nanoparticles

Neighbor	Coordination number (N)	Distance to neighbor shell, R (Å)	σ^2 (Å^{-2})
O_1	5.8 (6)	2.07 (1)	0.0076 (8)
Cr_1	4.7 (6)	3.16 (1)	0.009 (2)
Cr_2	3.2 (4)	3.47 (3)	0.012 (3)

range, at 5 K temperature. A nanoparticle sample weighing 30 mg was loaded inside a softgel capsule and subsequently placed inside the magnetometer for magnetic measurements. For the FC measurements, the field cooling was made using a field of 15000 Oe upon cooling from 330 to 5 K.

Results and discussion

Figure 1a shows an SEM image of the CSNs. Due to residual charges on the surface of the oxides, some of the CSNs tend to aggregate into bigger clumps. The SEM-EDX analysis shown in Fig. 1b confirms the elemental composition of the sample as Cr, Co, and O with a small contribution coming from the carbon in the conductive tape. Figure 1c shows the HR-TEM image of the core (α-Cr_2O_3 NPs) with ∼36 nm diameter. HR-TEM image of the CSNs, after the formation the Co-rich shell region, are presented in Fig. 1d and subsequently in Fig. 2 and in the ESM. The shell region can be clearly seen in Fig. 1d, where the interface of the core and the shell region is marked by a yellow dotted line.

In Fig. 2 we show high-resolution TEM (HR-TEM) analysis of a select α-Cr_2O_3@α-$Co_xCr_{2-x}O_y$ CSN. The distinct core and shell region are clearly identifiable. For this typical NP, the shell region extends to ∼6 nm. As shown in Fig. 2, the CSNs are crystalline throughout the core and shell regions, exhibiting continuity of atomic planes across the interface in epitaxial fashion. The close similarity of the fast Fourier transforms (FFTs) shown in Fig. 2 of the core and shell regions provides evidence of the continuity of the atomic registry throughout the NPs. The atomic interplanar spacing in the shell region, for the same types of planes, is slightly expanded as compared to the core region of the NPs. The TEM-EDX spectra show a higher percentage of Co present in the shell region of the NPs, whereas the core region is highly dominated by Cr (see Fig. 2). Some disorder, located primarily at the core–shell interface (see Fig. S3 in the ESM), in the form of vacancies, misfit

dislocations, stacking faults, and other defects that originate from the lattice mismatch between the core and shell is evident in the CSNs. This is also evident in the FFT's that are taken from the core, interface and shell regions (Fig. S3); the FFT taken from the interface region shows lattice-plane reflections but also a more diffuse halo. Interestingly, for the CSNs that exhibit faceted morphology, the presence or absence of nominal disorder appears to be facet-dependent (see Fig. 1d). We conjecture that the missing reflections observed in the FFT of the shell region seen in Fig. 2d (and Fig. S3) result from glide planes that may be formed due to slight re-orientations of MO_6 (M = Cr, Co) octahedra upon substitution of Co for Cr in the shell of the CSNs. However, further investigations are required in order to determine the full structural characteristics of our CSNs. Our previous studies suggest that the hydrothermal process involves partial dissolution of the NPs and co-deposition of the substitutional and host cations during the epitaxial growth of surface layers [35, 36].

The lattice parameters of the core and shell regions, and the volume-weighted mean size [37] of the CSNs, were determined from Rietveld refinement of the XRD data. The fit of the XRD data measured from the CSNs is shown in Fig. 3a. Structures of both the core and shell regions of the CSNs were determined from Rietveld refinement to conform to the corundum phase (space group #167:R$\bar{3}$c): The results from fitting are shown in Table S1 in the ESM. The sizes of the α-Cr_2O_3 NPs (prior to HNE) were estimated to be 39(2) nm across from the XRD and TEM analysis (also see Fig. S2 in the ESM). The size of the CSNs was estimated to be 52(4) nm based on TEM analysis and Rietveld refinement of the XRD data.

The fitting of the Co K-edge extended X-ray absorption fine structure (EXAFS) data is shown in Fig. 3b and the results are tabulated in Table 1. The EXAFS fitting results are consistent with Co substitution for Cr in solid solution leading to the formation of the $Co_xCr_{2-x}O_y$ phase with corundum structure in the CSNs. The first, second, and third shell distances are expanded by ∼4, 9, and 1 %,

respectively, surrounding Co relative to those surrounding Cr in the corundum structure ($R\bar{3}c$) of α-Cr_2O_3. The discrepancy in the second shell distance is likely due to interference from an intermediate shell of O atoms between the second and third shell Cr atoms surrounding Co. Nevertheless, the overall expansion of the near-neighbor distances is consistent with our structural results obtained from the analysis of the XRD data. The Co–O distance of 2.07 Å compares very well with the Co–O near-neighbor distance in octahedral coordination measured in Co-doped iron spinel NPs [38]. The somewhat larger σ^2 values are indicative of a slightly disordered local structural environment surrounding Co in the shell region, which is consistent with size mismatch between the Co^{2+} and Cr^{3+} ions along with the epitaxial growth-induced strain imposed upon the lattice structure of the shell.

The close match between the calculated and experimentally measured X-ray absorption near edge structure (XANES) shown in Fig. 4a is further evidence that the structural environment surrounding Co in the shell of CSNs is a corundum phase. The primary location in energy (7709.8 eV) of the pre-edge peak (Fig. 4a) is consistent with the +2

Figure 4 a The Co K-edge XANES measured from the CSNs (*blue line*) and the simulated curve generated using FEFF9 (*red line*); the inset shows the pre-edge peak (*blue line*-data points) and fit the pre-edge peak (*red line*); **b** The angular momentum projected density of states (*l*-DOS) calculated using FEFF9.

oxidation state of Co in the NPs. The pre-edge feature is primarily due to dipole-allowed Co 1s-electron transitions to unoccupied mixed or hybridized 3d (Co) and p (Co, O) states. The weak shoulder on the high-energy side is due to quadrupole-allowed Co 1s → 3d electronic transitions. The doublet-shaped low-intensity characteristics of the pre-edge peak is an indication of the crystal field (or molecular orbital) splitting of the Co 3d orbital sub-bands in an octahedrally (i.e., O_h symmetry) distorted structure of a CoO_6 polyhedral unit.

Fitting of the pre-edge feature yields 7709.8 eV for the dipole-allowed (A_1) and a 7711.6 eV value for the quadrupole-allowed (A_2) transition energies, respectively. These values are consistent with the A_1 and A_2 values of 7709.0 and 7711.7 eV, respectively, measured for Co^{2+} in octahedral site symmetry in $CoFe_2O_4$ [39].

The angular momentum projected density of states (*l*-DOS) calculation (Fig. 4b) shows that the pre-edge feature (labeled A) is dominated by d-DOS, but also has substantial p-DOS and s-DOS contributions. This is consistent with transition of 1s electrons to half-filled 3d-(s,p) hybridized or mixed states that result from (distorted) octahedral crystal field splitting effects. The *l*-DOS shows that the shoulder feature (B in Fig. 4b at ∼7718 eV) in the XANES is dominated by contribution from the s-DOS and has a substantial contribution from the p-DOS. In addition, our *l*-DOS calculations show that the white line (C) and the shoulder features (D and E) of the XANES are dominated by the p-DOS. This is indicative of dipole-allowed 1s to empty quasi-bound, continuum Co 4p-like state electronic transitions. Although the calculated *l*-DOS provides limited density of states information, namely that the final electronic states are consistent with the Co(II) ion situated in a local potential having distorted octahedral symmetry, full first principles calculations are required to gain a better picture of the electronic structure of the α-$Co_{0.38}Cr_{1.62}O_{2.92}$ nanophase compound at the shell of our CSNs.

The constituent atomic percentages of Cr, O, and Co were determined from analysis of the Cr $2p_{3/2}$, O 1s, Co $2p_{3/2}$ peaks, respectively, in the X-ray photoemission spectroscopy (XPS) survey scan (Fig. S6 in ESM) of our CSNs (see ESM for tabulation of results). Analysis of the Co $2p_{3/2}$ high-resolution peak shows that Co is in the +2 oxidation state (see Fig. 5 and ESM for details). The +2 oxidation state of Co in the
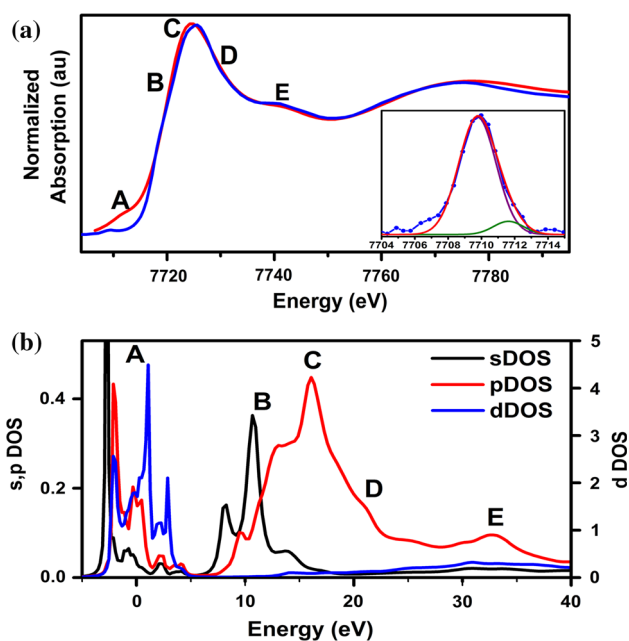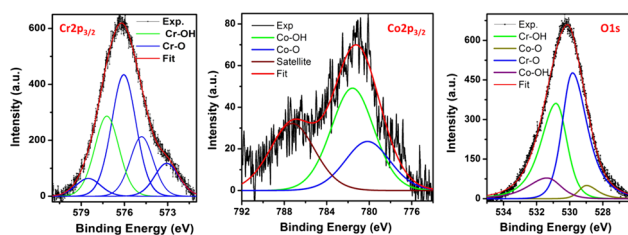
Figure 5 High-resolution XPS spectra measured from the α-Cr_2O_3@α-$Co_xCr_{2-x}O_y$ CSNs (*black line*) and fits (*colored lines*) to the data for Cr $2p_{3/2}$ (*left panel*), Co $2p_{3/2}$ (*middle panel*), and O 1s (*right panel*).
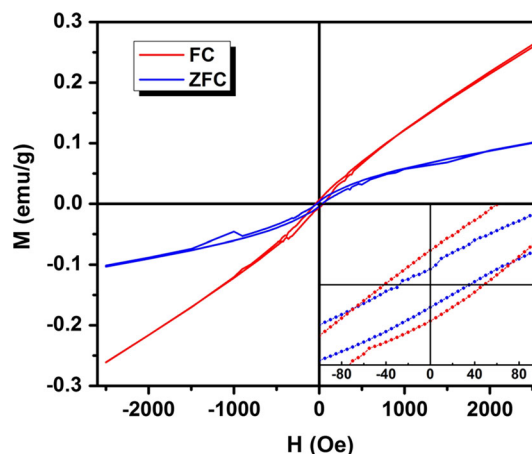

Figure 6 Zero field cooled (ZFC) and field cooled (FC) hysteresis loops, i.e., magnetization (M) versus applied magnetic field (H), measured from the CSNs. The *inset* shows the hysteresis loop FC and ZFC curves in the region close to 0 values in M and H.

NPs is consistent with a high-spin state $= 3/2$ due to the (distorted) octahedral crystal-field d-orbital splitting effects. Our XPS results provide evidence that the shell of the NPs is slightly oxygen deficient due to charge compensation upon substitution of Co^{2+} for Cr^{3+}. The EXAFS and XANES analyses of the CSNs are also consistent with a shell which is deficient in oxygen; the structural refinement of the XRD data was made to account for the oxygen deficiency. Thus, the stoichiometric formula determined for the shell regions of our CSNs is $Co_{0.38}Cr_{1.62}O_{2.92}$ (see ESM for details). To the best of our knowledge, this is the first report of a successful synthesis of a corundum-structured, Co(II)-containing non-equilibrium α-$Co_xCr_{2-x}O_y$ compound either in bulk or nanophase form. Bodade et al. [40] reported synthesis of Co-doped Cr_2O_3 NPs, but provided no direct evidence for Co incorporation, Co oxidation state, or the structure of the NPs. The synthesis of non-equilibrium heteroepitaxial $M_xCr_{2-x}O_{3-y}$ (M: Co, Ni, Fe, etc.) nanophases in chromia-based CSNs offers an opportunity to study and exploit their potentially novel magnetic and multifunctional properties.

Figure 6 shows magnetic hysteresis curves measured under zero field cooled (ZFC) and field cooled (FC) conditions in a magnetic field (H) ranging from -2.5 to $+2.5$ KOe. The FC or ZFC hysteresis curves do not reach saturation at up to ± 50 KOe. The value of the net coercivity, as defined using $H_C = |(H^+ - H^-)|$, where H^+ and H^- are the coercive fields for ascending and descending curves, is ~ 27 Oe greater for the FC curve vs the ZFC curve. This is consistent with a presence of FM/FiM ordering in the shell and AFM ordering in the core of the NPs and an exchange bias effect between the two [20]. We have recently synthesized α-Cr_2O_3@α-$Ni_{0.58}Cr_{1.42}O_{2.88}$ and α-Cr_2O_3@α-$Fe_{0.40}Cr_{1.6}O_{2.92}$ CSNs that show a substantially stronger exchange bias effect as evidenced in a

coercivity shift of ~ 100 and ~ 365 Oe, respectively. The substantial exchange bias fields result from the strong FM properties of the shells of these CSNs [41]. These results indicate that although the structural interface, size (i.e., overall and core vs shell), substitutional cation content, and shape properties are quite similar, the exchange bias properties are strongly dependent on the resultant magnetic properties of the $M_xCr_{2-x}O_{3-y}$ nanophase constituting the shells of the CSNs.

One of the outstanding issues in conventional CSNs is roughness of the core–shell interface, due to the dissimilarity of the core and shell structural phases. The interface roughness can result in a substantial spin anisotropy that can adversely affect the degree of exchange bias between the core and shell of the NPs [16]. The interface disorder coupled with interdiffusion can be so substantial as to warrant modeling of magnetic core–shell nanoparticles with an intermediate shell reflecting the interface layer [10]. Our HNE technique avoids the disorder effects imposed by the mismatch of dissimilar core vs shell structural phases, thereby producing a much sharper, well-defined core–shell interface which should have a strong impact on the interface magnetic anisotropy. This is expected to result in a greater control of design and more enhanced exchange bias effect between the AFM core and the FM or FiM shell in inverted CSNs synthesized using our HNE technique. The oxygen vacancies in the shell may play an important role in the magnetic properties of our CSNs. The oxygen vacancy-induced F-center

exchange, which occurs by F-center interaction with nearby cation spins, [42] has been shown to result in FM spin coupling in CeO_2 nanomaterials [43, 44]. In addition to its potential impact on the magnetic properties, the formation of oxygen vacancies may result in enhanced catalytic (i.e., photocatalysis) and gas sensing properties in our CSNs. Our HNE technique offers an opportunity to study the effect of overall size, shape, and core vs shell size effects on the magnetic properties of the CSNs. Studies on the effect of overall size on the magnetic properties of the CSNs are presently underway and will be reported in the future.

Conclusions

We have successfully synthesized a novel α-$Co_{0.38}$ $Cr_{1.62}O_{2.92}$ nanophase shell over a α-Cr_2O_3 core, to form inverted core–shell nanoparticles (CSNs) using our hydrothermal nanophase epitaxy (HNE) technique. The CSNs have a ~ 40 nm diameter core and a ~ 6 nm thick shell with a sharp and well-ordered core–shell interface. Our analysis indicates that the corundum structure of the nanoparticle is continuous in epitaxial fashion from the core to the shell with a slight expansion (~ 1 %) of the unit cell volume of the α-$Co_{0.38}Cr_{1.62}O_{2.92}$ shell, in comparison to that of the α-Cr_2O_3 core. Our magnetic measurements show evidence for an exchange bias effect between the FM/FiM shell and AFM core of the CSNs. Both the oxygen vacancies and the +2 oxidation state of Co (i.e., high-spin state = 3/2) may contribute toward the establishment of FM/FiM characteristics of the shell region. The HNE technique is a highly promising benign route for synthesis of novel nanophases having sharp interfaces and well-ordered core–shell structure. The synthesis of CSNs via the HNE method is a very exciting prospect for creation of novel magnetic, optical, and electronic nanomaterials as it affords the opportunity to synthesize new nanophases and nearly ideal CSNs.

Acknowledgements

Conflict of interest   The authors declare no conflict of interest.

References

[1] Borys NJ, Walter MJ, Huang J et al (2010) The role of particle morphology in interfacial energy transfer in CdSe/CdS heterostructure nanocrystals. Science 330:1371–1374. doi:10.1126/science.1198070

[2] Byers CP, Zhang H, Swearer DF et al (2015) From tunable core–shell nanoparticles to plasmonic drawbridges: active control of nanoparticle optical properties. Sci Adv 1:e1500988. doi:10.1126/sciadv.1500988

[3] Gawande MB, Goswami A, Asefa T et al (2015) Core–shell nanoparticles: synthesis and applications in catalysis and electrocatalysis. Chem Soc Rev 44:7540–7590. doi:10.1039/C5CS00343A

[4] Song S, Wang X, Zhang H (2015) CeO2-encapsulated noble metal nanocatalysts: enhanced activity and stability for catalytic application. NPG Asia Mater 7:e179. doi:10.1038/am.2015.27

[5] Xu C, Yuan Y, Cui A, Yuan R (2012) In situ controllable synthesis of Ag@AgCl core–shell nanoparticles on graphene oxide sheets. J Mater Sci 48:967–973. doi:10.1007/s10853-012-6823-2

[6] Si PZ, Zhang M, Zhang ZD et al (2005) Synthesis and structure of multi-layered WS2(CoS), MoS2(Mo) nanocapsules and single-layered WS2(W) nanoparticles. J Mater Sci 40:4287–4291. doi:10.1007/s10853-005-2797-7

[7] Wang J, Zeng XC (2009) Core–shell magnetic nanoclusters. In: Liu JP, Fullerton E, Gutfleisch O, Sellmyer DJ (eds) Nanoscale Magn Mater Appl. Springer, Berlin, pp 35–65

[8] Silva A, Silva-Freitas É, Carvalho J et al (2012) Magnetic particles in biotechnology: from drug targeting to tissue engineering. In: Petre M (ed) Advances in applied biotechnology. http://www.intechopen.com/books/advances-in-applied-biotechnology/magnetic-particles-in-biotechnology-from-drug-targeting-to-tissue-engineering

[9] López-Ortega A, Estrader M, Salazar-Alvarez G et al (2015) Applications of exchange coupled bi-magnetic hard/soft and soft/hard magnetic core/shell nanoparticles. Phys Rep 553:1–32. doi:10.1016/j.physrep.2014.09.007

[10] Juhin A, López-Ortega A, Sikora M et al (2014) Direct evidence for an interdiffused intermediate layer in bi-magnetic core–shell nanoparticles. Nanoscale 6:11911–11920. doi:10.1039/C4NR02886D

[11] Nogués J, Skumryev V, Sort J et al (2006) Shell-driven magnetic stability in core–shell nanoparticles. Phys Rev Lett 97:157203. doi:10.1103/PhysRevLett.97.157203

[12] Fontaíña Troitiño N, Rivas-Murias B, Rodríguez-González B, Salgueiriño V (2014) Exchange bias effect in CoO@Fe$_3$O$_4$ core–shell octahedron-shaped nanoparticles. Chem Mater 26:5566–5575. doi:10.1021/cm501951u

[13] Margaris G, Trohidou KN, Nogués J (2012) Mesoscopic model for the simulation of large arrays of bi-magnetic core/shell nanoparticles. Adv Mater 24:4331–4336. doi:10.1002/adma.201200615

[14] Mao Z, Zhan X, Chen X (2012) Defect-tuning exchange bias of ferromagnet/antiferromagnet core/shell nanoparticles by numerical study. J Phys Condens Matter 24:276002. doi:10.1088/0953-8984/24/27/276002

[15] Dimitriadis V, Kechrakos D, Chubykalo-Fesenko O, Tsiantos V (2015) Shape-dependent exchange bias effect in magnetic nanoparticles with core–shell morphology. Phys Rev B 92:64420. doi:10.1103/PhysRevB.92.064420

[16] Evans RFL, Bate D, Chantrell RW et al (2011) Influence of interfacial roughness on exchange bias in core–shell nanoparticles. Phys Rev B 84:92404. doi:10.1103/PhysRevB.84.092404

[17] Shore M, Fowler AD (1996) Oscillatory zoning in minerals; a common phenomenon. Can Mineral 34:1111–1126

[18] Jamtveit B (1999) Crystal growth and intracrystalline zonation patterns in hydrothermal environments. In: Jamtveit B, Meakin P (eds) Growth dissolution pattern form. Geosystems, Springer, pp 65–84

[19] Golosovsky IV, Salazar-Alvarez G, López-Ortega A et al (2009) magnetic proximity effect features in antiferromagnetic/ferrimagnetic core–shell nanoparticles. Phys Rev Lett 102:247201. doi:10.1103/PhysRevLett.102.247201

[20] Vasilakaki M, Trohidou KN, Nogués J (2015) Enhanced magnetic properties in antiferromagnetic-core/ferrimagnetic-shell nanoparticles. Sci Rep 5:9609. doi:10.1038/srep09609

[21] Farzaneh F (2011) Synthesis and characterization of Cr$_2$O$_3$ nanoparticles with triethanolamine in water under microwave irradiation. J Sci Islam Repub Iran 22:329–333

[22] McCart PA, Farris L, Mayanovic RA, Yan H. Investigations of TiO2 nanoparticles surface-doped with Eu in aqueous fluids to high P-T conditions. Symp DDD—Extreme Environ Route Nov Mater. 2013 doi:10.1557/opl.2013.1141

[23] (2008) TOPAS V4: General profile and structure analysis software for powder diffraction data. User's Manual. Bruker AXS, Karlsruhe, Germany

[24] Cheary RW, Coelho A (1992) A fundamental parameters approach to X-ray line-profile fitting. J Appl Crystallogr 25:109–121. doi:10.1107/S0021889891010804

[25] Coelho AA (2003) Indexing of powder diffraction patterns by iterative use of singular value decomposition. J Appl Crystallogr 36:86–95. doi:10.1107/S0021889802019878

[26] Thompson P, Cox DE, Hastings JB (1987) Rietveld refinement of Debye-Scherrer synchrotron X-ray data from Al$_2$O$_3$. J Appl Crystallogr 20:79–83. doi:10.1107/S0021889887087090

[27] Finger LW, Cox DE, Jephcoat AP (1994) A correction for powder diffraction peak asymmetry due to axial divergence. J Appl Crystallogr 27:892–900. doi:10.1107/S0021889894004218

[28] Campbell BJ, Evans JSO, Perselli F, Stokes HT (2007) Rietveld refinement of structural distortion-mode amplitudes. Ed Newsl No 8:81

[29] Campbell BJ, Stokes HT, Tanner DE, Hatch DM (2006) ISODISPLACE: a web-based tool for exploring structural distortions. J Appl Crystallogr 39:607–614. doi:10.1107/S0021889806014075

[30] Dinnebier R, Müller M (2012) Modern Rietveld refinement, a practical guide. In: Mittemeijer EJ, Welzel U (eds) Modern diffraction methods. Wiley-VCH Verlag GmbH & Co. KGaA, Weinheim, Germany

[31] Ravel B, Newville M (2005) ATHENA, ARTEMIS, HEPHAESTUS: data analysis for X-ray absorption spectroscopy using IFEFFIT. J Synchrotron Radiat 12:537–541. doi:10.1107/S0909049505012719

[32] Newville M (2001) IFEFFIT: interactive XAFS analysis and FEFF fitting. J Synchrotron Radiat 8:322–324. doi:10.1107/S0909049500016964

[33] Rehr JJ, Kas JJ, Prange MP et al (2009) Ab initio theory and calculations of X-ray spectra. Comptes Rendus Phys 10:548–559. doi:10.1016/j.crhy.2008.08.004

[34] Hedin L, Lundqvist BI (1971) Explicit local exchange-correlation potentials. J Phys C Solid State Phys 4:2064. doi:10.1088/0022-3719/4/14/022

[35] Mayanovic RA, Yan H, Anderson AJ et al (2012) In situ X-ray absorption spectroscopic study of the adsorption of

Ni2+ on Fe3O4 nanoparticles in supercritical aqueous fluids. J Phys Chem C 116:2218–2225. doi:10.1021/jp2067793

[36] Yan H, Mayanovic RA, Demster JW, Anderson AJ (2013) In situ monitoring of the adsorption of Co2+ on the surface of Fe3O4 nanoparticles in high-temperature aqueous fluids. J Supercrit Fluids 81:175–182. doi:10.1016/j.supflu.2013.05.017

[37] Balzar D, Audebrand N, Daymond MR et al (2004) Size-strain line-broadening analysis of the ceria round-robin sample. J Appl Crystallogr 37:911–924. doi:10.1107/S0021889804022551

[38] Carta D, Casula MF, Falqui A et al (2009) A structural and magnetic investigation of the inversion degree in ferrite nanocrystals MFe2O4 (M = Mn Co, Ni). J Phys Chem C 113:8606–8615. doi:10.1021/jp901077c

[39] Yan H, Mayanovic RA, Demster J, Anderson AJ. In situ XANES Study of Co2 + Ion Adsorption on Fe3O4 Nanoparticles in Supercritical Aqueous Fluids. Symp—Mater Chall Curr Future Nucl Technol. 2012 doi: 10.1557/opl.2012.183

[40] Bodade AB, Rohokale PG, Padole PR (2011) Electrical and gas sensing properties of chemically modified nanocrystalline Cr_2O_3 based H_2S sensor. Nano Trends J Nanotech Appl 11:18–21

[41] Hossain MD, Dey S, Mayanovic RA, Benamara M (2016) Structural and magnetic properties of well-ordered inverted core–shell α-Cr_2O_3/α-$MxCr_{2-x}O_3$ (M = Co, Ni, Mn, Fe) Nanoparticles. MRS Adv. doi:10.1557/adv.2016.324

[42] Chandra S, Khurshid H, Li W et al (2012) Spin dynamics and criteria for onset of exchange bias in superspin glass Fe/γ-Fe_2O_3 core–shell nanoparticles. Phys Rev B 86:14426. doi:10.1103/PhysRevB.86.014426

[43] Fernandes V, Mossanek RJO, Schio P et al (2009) Dilute-defect magnetism: origin of magnetism in nanocrystalline CeO_2. Phys Rev B 80:35202. doi:10.1103/PhysRevB.80.035202

[44] Phokha S, Pinitsoontorn S, Maensiri S (2013) Structure and magnetic properties of monodisperse Fe^{3+}-doped CeO_2 nanospheres. Nano-Micro Lett 5:223–233. doi:10.1007/BF03353753